



Full Length Article

Microstructure analyses and phase-field simulation of partially divorced eutectic solidification in hypoeutectic Mg-Al Alloys

Joo-Hee Kang^a, Jiwon Park^{a,*}, Kyung Song^a, Chang-Seok Oh^a, Oleg Shchyglo^b, Ingo Steinbach^b^a Korea Institute of Materials Science, Changwon 51508, Republic of Korea^b Interdisciplinary Centre for Advanced Materials Simulation, Ruhr-University Bochum, 44801 Bochum, Germany

Received 14 July 2020; received in revised form 11 March 2021; accepted 9 April 2021

Available online 16 June 2021

Abstract

In this study the partially divorced eutectic microstructure of α -Mg and β -Mg₁₇Al₁₂ was investigated by electron backscatter diffraction, transmission electron microscopy, and phase-field modeling in hypoeutectic Mg-Al alloys. The orientation relationships between the individual eutectic α grains, eutectic β phase, and primary α grains were investigated. While the amount of eutectic morphology is primarily determined by the Al content, the in-depth microstructure analyses and the phase-field simulation suggest non-interactive nucleation and growth of eutectic α phase in the β phase grown on the interdendritic primary α dendrites. Also, phase-field simulations showed a preferred nucleation sequence where the β phase nucleates first and subsequently triggers the nucleation of eutectic α phase at the moving β phase solidification front, which supports the microstructural analysis results.

© 2021 Chongqing University. Publishing services provided by Elsevier B.V. on behalf of KeAi Communications Co. Ltd.

This is an open access article under the CC BY-NC-ND license (<http://creativecommons.org/licenses/by-nc-nd/4.0/>)

Peer review under responsibility of Chongqing University

Keywords: Mg-Al alloy; Partially divorced eutectic; Solidification; Electron backscatter diffraction; Phase-Field modeling.

1. Introduction

In the majority of cast Mg alloys containing more than 2 atomic% Al, eutectic microstructures composed of α -Mg and β -Mg₁₇Al₁₂ are readily formed during solidification. Their morphologies vary prominently from fully divorced eutectic through several intermediate structures to eutectic lamellar depending on the cooling rate and the content of the alloying elements [1–5]. The importance of the β phase morphology on the mechanical and electrochemical properties of Mg-Al alloys has been discussed in several studies [6–8]. The control of fraction, distribution and shape of the eutectic constituents and their overall morphology are crucial in optimizing the mechanical properties and the corrosion resistance of the alloys because the intermetallic β phase is brittle and electrochemically more noble than the α phase. In addition, the nucleation and growth of the β phase in an interdendritic liquid between

primary α phase dendrites occur at the last stage of solidification and is closely related to hot-tearing, which could be prevented by providing an open feeding path in the liquid channel. In view of its technical importance, it is necessary to have an improved understanding of how the eutectic microstructure is formed.

In Mg-Al alloys, the eutectic fraction is primarily determined by the Al content. While the maximum solubility limit of Al in the α phase is 11% [9] (hereafter, in atomic%) to form an equilibrium single α phase during solidification, the metastable eutectic microstructure can be formed in the non-equilibrium solidification of alloys containing less than 11% of Al. Liquid phase readily enriched with solute over the solubility limit during technical non-equilibrium alloy solidification [10] which enters eutectic-forming region in phase diagram. The solidification sequence follows the formation of the primary α phase (hereafter, α_p), and thereafter, the eutectic β phase and α phase (hereafter, α_e) in the interdendritic channel of α_p . In addition to the Al content, the cooling rate and other alloying components such as Zn also affect the spe-

* Corresponding author.

E-mail address: jiwonp@kims.re.kr (J. Park).

cific morphology of the eutectic region. Dahle et al. [2] reported a drastic change in the eutectic structure within a single β grain along the growth direction in a directionally solidified Mg-9.1Al-0.4Zn alloy. The rapid morphological transition from fully divorced β through the partially divorced eutectic structure with thick β halo to fibrous and lamellar eutectics with thin β halo occurred within several tens of μm . The result emphasizes the importance of temperature control in accomplishing the desired microstructure and in understanding the underlying mechanisms of divorced eutectics. To achieve quantitative comparisons of different cooling conditions and to obtain simulation results reflecting actual microstructure evolution, this study conducted direct temperature measurement of the melt during the solidification process.

This study compares partially divorced eutectic morphologies of equiaxed Mg-Al alloys containing 5–15% Al with different cooling rates. Thorough microstructural analyses were conducted by optical microscopy to observe the overall casting microstructure and by transmission electron microscopy (TEM) for a comprehensive investigation of the individual phases and grains. The partially divorced eutectic microstructure developed during the interdendritic solidification of the residual liquid pocket was simulated using the phase-field approach and compared with the experimental microstructure.

1.1. Experiments

Mg-Al alloys containing 5%, 10%, and 15% Al were prepared with reagent grade metal granules and melted in an induction furnace under protective CO_2 and SF_6 atmospheres up to 973 K. Thereafter, the melt was poured into the preheated (523 K) steel mold with Type-K thermocouples placed inside the mold. The wedge-shaped mold was adopted to obtain two different cooling rates from a single heat to reduce the compositional variation as shown in Fig. 1. The analyzed microstructure specimens were taken from the volume close to the thermocouples, which assures quantitative assessment of the cooling rate effect and provides reasonable input parameters for the phase-field simulations.

The casting microstructures were analyzed by polarized light microscopy (PM), scanning electron microscopy (SEM), electron backscatter diffraction (EBSD), and TEM in diverse scales. The PM specimens were etched with 4.2 g of picric acid, 10 mL of acetic acid, 700 mL of ethanol, and 10 mL of distilled water mixture etchant. The SEM and EBSD specimens were mounted, ground and polished to colloidal silica suspensions finish. SEM and EBSD examinations were carried out using JEOL JSM-7001F and JSM-7900F field emission SEM, both equipped with Oxford EBSD (NordlysNano and Symmetry) and energy dispersive spectroscopy (EDS). The EBSD maps and EDS data were analyzed using Oxford Aztec 4.2 and TSL OIM 8.0 software to produce orientation maps, pole figures, and elemental profiles. TEM specimen was prepared using a focused ion beam (FIB, Carl Zeiss AURIGA Dual-Beam) from the pre-analyzed EBSD specimen to obtain the designated specimen orientation. Selected area diffraction

patterns (SADP) and EDS profiles were acquired in JEOL JEM-2100F field emission TEM equipped with Oxford EDS.

2. Phase-field modeling

The multi-phase-field approach with a locally linearized phase diagram scheme was applied to simulate the solidification microstructure evolution during the eutectic condition [11–14]. In this approach, each grain/phase is assigned a distinct phase-field parameter, $\varphi_p(x,t) \in [0, 1]$. The evolution of the phase-field parameter is described by the following equations:

$$\dot{\phi}_i = \sum_{j=1}^N \frac{M_{ij}}{N} \left(\sum_{k=1}^N (\gamma_{jk} - \gamma_{ki}) I_k + \frac{\pi^2}{8\eta} \Delta G_{ij} \right) \quad (1)$$

$$I_k = \nabla^2 \phi_k + \frac{\pi^2}{\eta^2} \phi_k \quad (2)$$

where M_{ij} is the interface mobility between phase i and j , N is the local number of the non-vanishing phase-field, η is the interface thickness, and ΔG_{ij} is the thermodynamic driving force. The anisotropic interface energy, $\gamma_{\alpha - liq}$, is used for the interface between α and the liquid phases following the approach from Böttger et al. [15]. For the interface between the β and liquid, as well as the β and α , isotropic interface energy is used. The evolution of the composition, \dot{c} , is described by the following diffusion equation:

$$\dot{c} = \nabla \left(\sum_{i=1}^N \phi_i (D_i \nabla c_i) + \sum_{i,j=1}^N j_{ij} \right) \quad (3)$$

where D_i is the diffusion coefficient of the solute and j_{ij} is the anti-trapping current [14]. The phase-field equation given above were discretized using the finite difference scheme. The heat extracted upon cooling is balanced with the heat of phase transformation as provided below:

$$\rho c_p \dot{T} = \sum_{n_{xyz}} \sum_{i \neq j} \dot{\psi}_{ij} L_{ij} + \dot{Q} \quad (4)$$

where ρ is density, c_p is the heat capacity, n_{xyz} is the discrete volume element, $\dot{\psi}_{ij}$ is the local transformation rate between pair-wise phases i and j defined by $\dot{\phi}_i = \sum_{j \neq i}^N \dot{\psi}_{ij}$, L_{ij} is the latent heat released during the phase transformation, and \dot{Q} is the heat extraction rate.

The nucleation model was adopted from Greer et al. [16], which determines the onset of the nucleation and growth of a seed corresponding to the achieved undercooling. The seeds of each phase were randomly distributed over the simulation domain with their size following the normal distribution (only the positive tail of the distribution is used),

$$N(d) = \frac{N_0}{\sigma \sqrt{2\pi}} \exp \left(-\frac{1}{2} \left(\frac{d - \mu}{\sigma} \right)^2 \right) \quad (5)$$

where N_0 is the nucleation seed density, d is the seed diameter, μ is the center of the distribution, and σ is its standard deviation. The numerical parameters used in the simulation are listed in Table 1.

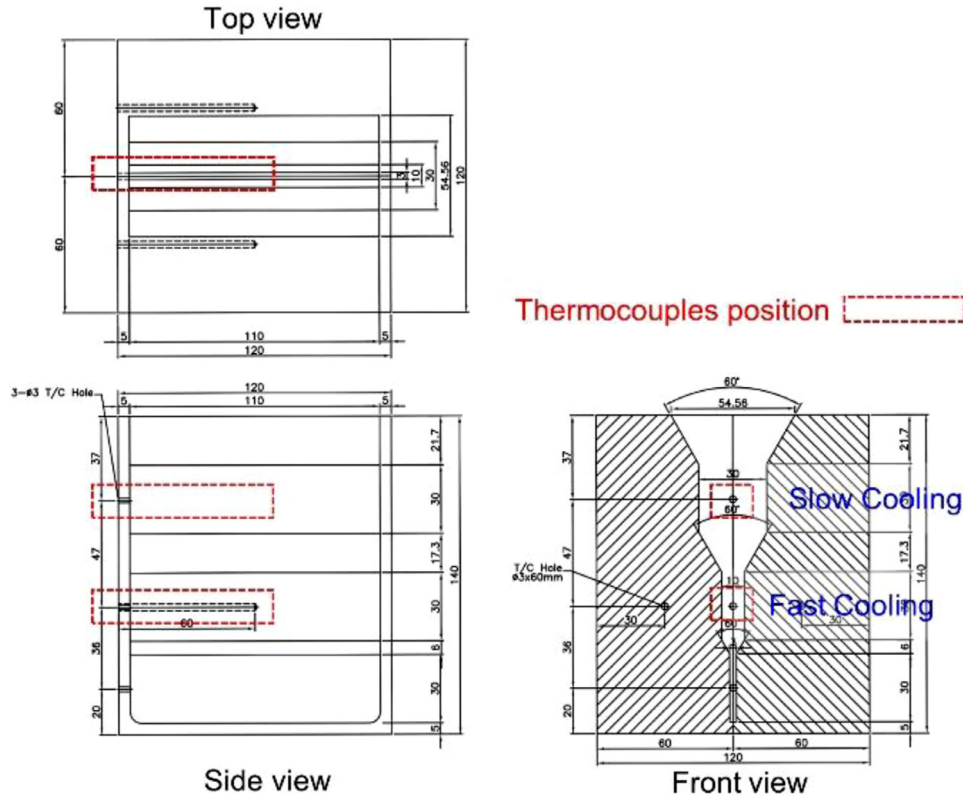


Fig. 1. Experimental set-up.

Table. 1
List of simulation parameters.

Parameterx	Symbol	Value	Unit
Liquidus slope	$m_{\text{liq-}\alpha}$	-6.90	K /%
	$m_{\text{liq-}\beta}$	3.50	K /%
Solidus slope	$m_{\alpha\text{-liq}}$	-27.58	K /%
	$m_{\beta\text{-liq}}$	9.00	K /%
Solvus slope	$m_{\alpha\text{-}\beta}$	-22.40	K /%
	$m_{\beta\text{-}\alpha}$	-103.00	K /%
Intersection concentration	$C_{\alpha\text{-liq}}$	0.00	%
	$C_{\beta\text{-liq}}$	45.64	%
	$C_{\alpha\text{-}\beta}$	34.20	%
Intersection temperature	$T_{\alpha\text{-liq}}$	923.15	K
	$T_{\beta\text{-liq}}$	760.60	K
	$T_{\alpha\text{-}\beta}$	1301.84	K
Nucleation seed density	N_0^α	5.0×10^{15}	m^{-3}
	N_0^β	1.5×10^{16}	m^{-3}
Mean diameter of the seeds	μ	-1.5×10^{-7}	M
Standard deviation	σ	1.0×10^{-7}	M
Interface energy	$\gamma_{\alpha\beta}$	0.09	J/m ²
Diffusion coefficient	$D_{\text{Al}}^{\text{liq}}$	3.9	m ² /s
	$D_{\text{Al}}^\alpha, D_{\text{Al}}^\beta$	3.9×10^{-3}	m ² /s
Diffusion activation energy	$Q_{\text{Al}}^{\text{liq}}, Q_{\text{Al}}^\alpha, Q_{\text{Al}}^\beta$	1.55×10^5	J/mol
Entropy of fusion	ΔS_f^α	-1.0×10^6	J/m ³ •K
	ΔS_f^β	-1.2×10^6	J/m ³ •K

3. Results and discussion

In the as-cast microstructures of specimens with various Al contents and cooling rates shown in Fig. 2, equiaxed grain refinement is evident with an increase in the Al content and

cooling rate. The addition of Al promotes the formation of the eutectic structure consisting of β and eutectic α_e phases in the interdendritic channel between primary α_p dendrites. The fractions of the eutectic region in Fig. 2(a) and 3 in fast cooling condition are in reasonable agreement with the calculated solid fractions of 7, 18, and 31 mol% for 5%, 10%, and 15% Al specimens from the Scheil-Gulliver solidification model using TCMG2 [17] database in Thermo-Calc [18]. The actual eutectic fraction also depends on the cooling rate [5] since the phase transformation is controlled by the solute diffusion in diffusion-controlled eutectic solidification scheme [10]. Previous works [12,13] by two of the current authors examined the effect of the cooling rate on the eutectic volume fraction using phase-field modeling. This study focuses on the Al content which has a significant impact on the morphology changes from the (partially) divorced eutectic to the coupled eutectic microstructure as shown in Fig. 3. In the SEM micrographs, the bright region indicates the β phase and the dark phase indicates the α phase. The light hue around the β phase inside the dark α phase indicates the Al enrichment in the interdendritic region which often transforms into continuous and discontinuous precipitations.

As the Al content increases, the eutectic morphology changes from a fully divorced (5% Al) structure to a partially divorced (10–15% Al) structure [1–3]. Microsegregation of Al in the liquid pocket isolated between the α_p dendrites allows the formation of the β phase even if the initial composition of the alloy (5% Al) is far below the maximum solubility limit of Al in the α phase, which is 11% at the eutectic temper-

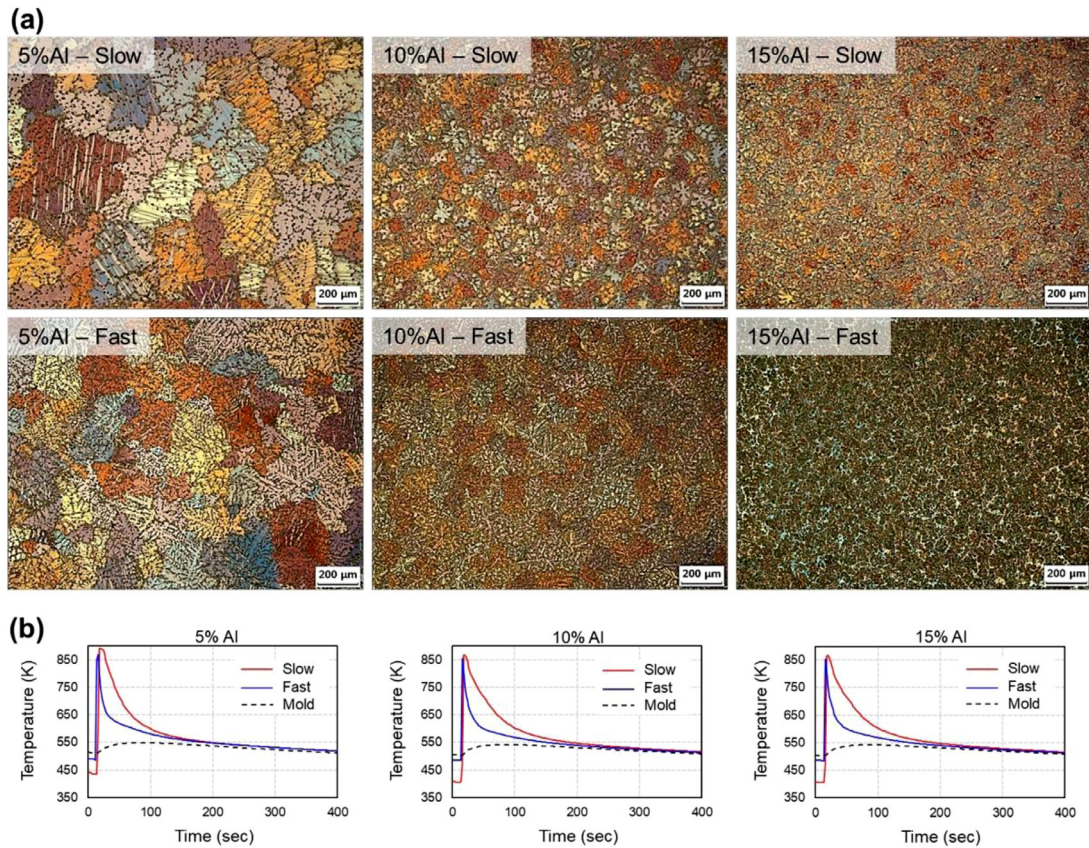


Fig. 2. (a) PM micrographs showing as-cast grain morphologies corresponding to different Al contents and cooling rates and (b) cooling curves of the specimens directly measured in the melts. (For interpretation of the references to colour in this figure legend, the reader is referred to the web version of this article.)

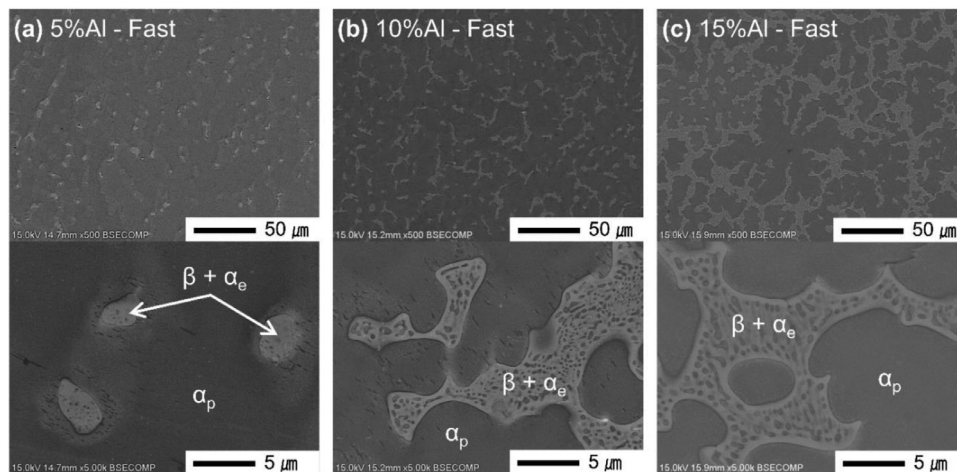


Fig. 3. SEM micrographs of the primary and eutectic microstructures of the fast-cooled specimens containing (a) 5% Al (b) 10% Al (c) 15% Al.

ature. As the eutectic fraction increases with the Al content, its morphology undergoes a prominent transition from isolated globular grains to interconnected networks. The convex curvature of the β grains in Fig. 3(a) changes to the mixture of convex and concave in (b) and finally to the fully concave structure in (c), which suggests that the solidification of the β grains with convex shape is completed before the α_p den-

drite reaches them. It is also noticeable that the halo of β is formed along the perimeter of the eutectic region.

The size of the β grain can be estimated from the comparison between the orientation and the phase maps in the EBSD analyses shown in Fig. 4. The isolated and partially connected β grains in Fig. 4(a,b) grow up to approximately 20 μm as single grains. Conversely, the eutectic network which spans

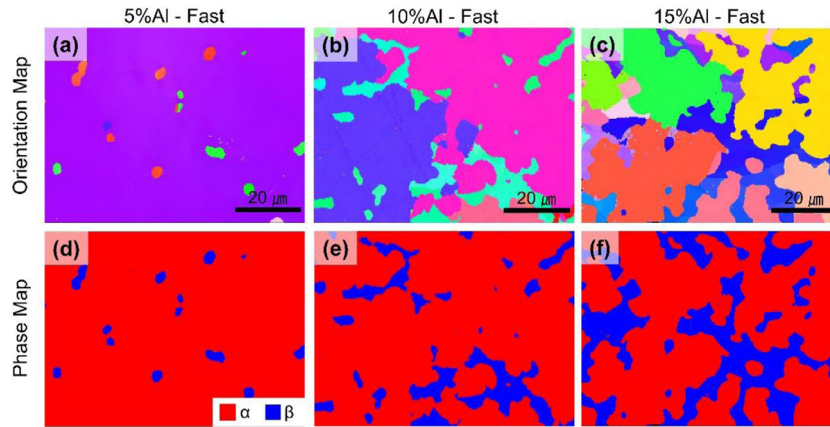


Fig. 4. EBSD orientation maps (a-c) and phase maps (d-f, red: α phase, blue: β phase) of (a, d) 5% Al (b, e) 10% Al (c, f) 15% Al. (For interpretation of the references to colour in this figure legend, the reader is referred to the web version of this article.)

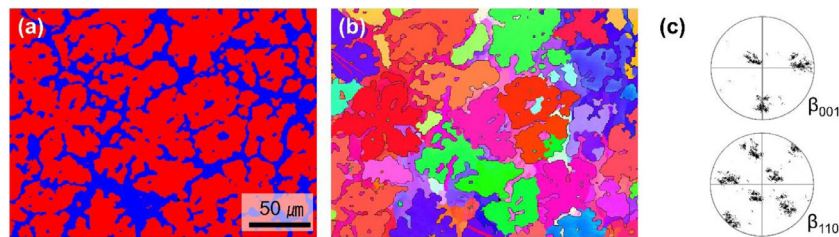


Fig. 5. Large-area EBSD maps of 15% Al specimen (a) phase map (red: α phase, blue: β phase), (b) orientation map (c), and (001) and (110) pole figures of β from (b). (For interpretation of the references to colour in this figure legend, the reader is referred to the web version of this article.)

over several tens of μm consists of multiple β grains in Fig. 4(c). Due to the effective resolution limit of the EBSD analysis, the α_e grains inside the β grains are not visible in the low-magnification EBSD analysis. However, the large-area EBSD maps of the 15% Al specimen and the corresponding (001) and (110) pole figures of the β grains in Fig. 5 confirm that the orientation of the β grains does not significantly differ. Such a similar but discrete distribution of the β orientations could be due to the independent nucleation events in a locally confined thermal condition. The β halo stretched over multiple grains in the eutectic region can be explained by the preferential growth of the β phase along the α_p perimeter where the Al rejected from the growing α_p front is piled-up. The β phase grows by consuming Al in the liquid, and reduces the Al composition of the melt allowing the formation of α_e in a eutectic manner. The EDS composition profile of a partially divorced grown β and α_e of the 10% Al specimen in Fig. 6 shows a smooth transition of the Al profile across the α_p/β boundary.

In technical Mg alloys, increasing the cooling rate, decreasing the Al content, and increasing the Zn content are known to promote divorced eutectic morphology by reducing the amount of eutectic region developed at the end of the solidification sequence. Meanwhile only weak evidence of the (partially) divorced eutectics was presented, which can distinguish between divorced eutectics and isolated coupled growth, mainly due to the limitation of the technical resolution. In addition to the regular eutectic morphology, the isolated secondary phase (α_e in this case) can be grown in a eutectic

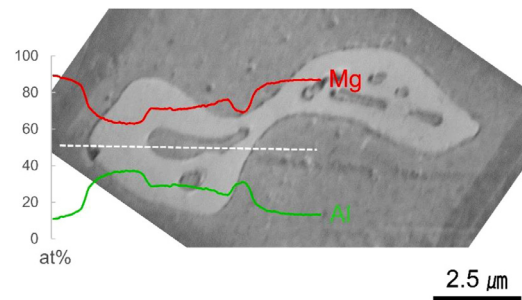


Fig. 6. EDS composition profile of a β grain in 10% Al specimen.

manner with rod/irregular lamellar shapes [19–21]. In addition to the detached growth, divorced eutectics rarely incorporate the interactions between two eutectic phases such as solutal exchange or orientation relationship (OR). A thorough literature review reveals the occurrence of highly non-spherical β grain at the α grain boundary or in the bulk of the α with six preferential ORs in the solid-solid phase transformation [22–25] and one relationship in directional solidification [26]. While these crystallographic relationships are not reported in the equiaxed solidification structure, they could indicate a preferred orientation of a nucleus at the interface to the opposite phase. Table 2 shows the list of previously reported ORs between the α and β phases. To examine possible ORs between the eutectic β and α_e grains, seven reported ORs are checked in a partially divorced eutectic region of the 10% Al specimen using EBSD. In Fig. 7(b-h), the red lines in each map

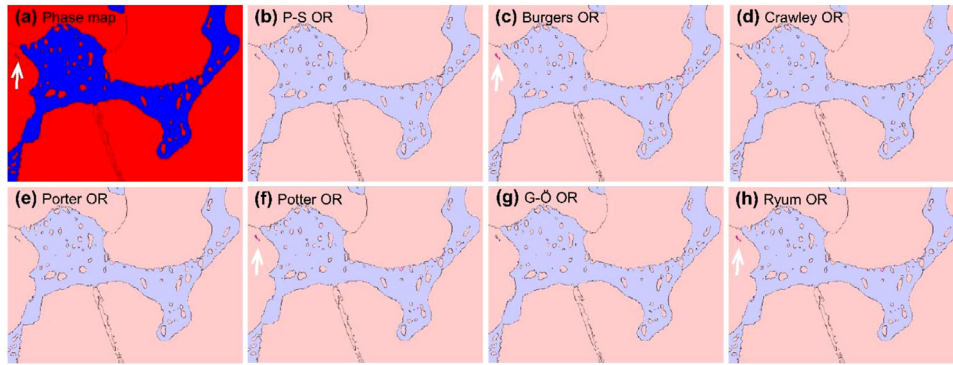


Fig. 7. Seven reported ORs between the α and β phases (a) EBSD phase map of a partially divorced eutectic region in 10% Al specimen (b) Pitsch-Schrader OR (c) Burgers OR (d) Crawley OR (e) Porter OR (f) Potter OR (g) Gjønnes-Östmoen OR (h) Ryum OR.

Table. 2
List of ORs between the α and β phases.

OR	Direction	Plane	Reference
Pitsch-Schrader	$[100]_{\beta} \parallel [2\bar{1}\bar{1}0]_{\alpha}$	$(011)_{\beta} \parallel (0001)_{\alpha}$	[23]
Burgers	$[\bar{1}\bar{1}\bar{1}]_{\beta} \parallel [2\bar{1}\bar{1}0]_{\alpha}$	$(011)_{\beta} \parallel (0001)_{\alpha}$	[22–24]
Crawley	$[211]_{\beta} \parallel [2\bar{1}\bar{1}0]_{\alpha}$	$(1\bar{1}\bar{1})_{\beta} \parallel (0001)_{\alpha}$	[22]
Porter	$[\bar{2}55]_{\beta} \parallel [2\bar{1}\bar{1}0]_{\alpha}$	$(511)_{\beta} \parallel (0001)_{\alpha}$	[22]
Potter	$[1\bar{1}\bar{1}]_{\beta} \parallel [2\bar{1}\bar{1}0]_{\alpha}$	$(011)_{\beta} \parallel (0001)_{\alpha}$	[23,25]
Gjønnes-Östmoen	$[2\bar{1}\bar{1}]_{\beta} \parallel [2\bar{1}\bar{1}0]_{\alpha}$	$(011)_{\beta} \parallel (0001)_{\alpha}$	[22]
Ryum	$[111]_{\beta} \parallel [11\bar{2}0]_{\alpha}$	$(10\bar{1})_{\beta} \parallel (1101)_{\alpha}$	[26]

indicate the matching boundaries with OR and the gray lines indicate the phase boundaries without OR. When these ORs are checked in EBSD within five degrees of tolerance for both planes and directions, the results reveal that no reported OR occurs between the eutectic β and α_e phases. Whereas the α_p and β phases show some matching ORs as indicated with the white arrows in Fig. 7, which corresponds to the precipitation in the solid state.

Further analyses were conducted for 40 α_e grains on the surface of the specimen in Fig. 7 and for three grains beneath the surface with respect to the adjacent α_p and β grains. The vertical sectioning using FIB confirms that the α_e grains are not part of the fibrous eutectic morphology as shown in Fig. 8(a). The spatial arrangement of the grains and their relative orientations were determined by the stepwise angle records from the EBSD orientation maps, the FIB sectioning in the designated cutting angle close to the $[0001]$ zone-axis of the α_p grain in the target region, and the specimen tilting in the TEM analysis. The SADP micrographs of the α_e grains buried under the surface in Fig. 8(a) show that grain 1 and 2 are close to the $[0001]$ zone-axis but rotated in the plane by 2.18° with respect to each other. Conversely, the c-axis of the grain 3 is slightly misaligned with respect to the beam incident direction and that of grain 1 and 2. The zone axis patterns inside the α_e grains in Fig. 8(a) also indicate that these grains are of a different orientation. Fig. 8(d) shows the SADP micrographs of the α_p and β grains adjacent to the α_e in Fig. 8(a).

When the orientation of the α_e grains on the surface is compared to the adjacent α_p grain marked as point 9 in Fig. 8(b), each α_e grain shows a high misorientation angle

with a maximum of 65° as presented in the (0001) pole figure in Fig. 8(f). In Fig. 8(e), relative orientations of the α_e grains determined in the TEM and EBSD analyses are represented with hexagonal unit cells. Such a weak relationship between the α_e grains suggests non-interactive nucleation and growth of the β and α_e grains, which are the crucial factors in divorced eutectic morphology. While each of the α_e grains has different orientations, some neighboring grains exhibit associated arrangements within a few degrees which might be a result of the similar thermal conditions analogous to the β grains in Fig. 5(c).

The absence of the solutal exchange in the divorced eutectic determines the characteristic morphology of the α_e grains in its chemistry and shape. Fig. 9 compares the Al distribution between the α_e and α_p grains, which display a flat Al concentration profile within the α_e grain that is lower than the eutectic composition (Fig. 9(a)). Conversely, Fig. 9(b) shows that Al is enriched in the last solidified region owing to the solutal rejection from the growing α_p front. During eutectic solidification the nucleation of the α_e phase can be promoted if sufficient Al is consumed by the growing β phase and the Al concentration in the liquid drops below the eutectic composition. When the α_e phase grow cooperatively with the β phase, gradual concentration changes in the adjacent α_e and β grains are observed with the highest Al concentration at the α/β boundary as shown in Figs. 6 and Fig. 9(b). However, sharp concentration changes on the α_e/β interface and the flat distribution of Al in Fig. 9(a) indicate that the α_e and β are grown without a solutal exchange in the divorced eutectic scheme.

To understand the competition between cooperative growth and the nucleation-dominated formation of the divorced eutectic structure, phase-field simulations were performed. The detailed simulation scheme was provided in previous works [12,13]. This study concentrates on simulating the remaining liquid pockets in the α_p interdendritic region near eutectic temperature. The simulation started from a residual liquid pocket with the eutectic composition surrounded by the α_p phase. The system was cooled starting from the eutectic temperature with the experimentally determined cooling rate of 25 K/s for the 10% Al-Fast specimen in Fig. 2(b). The α_p was still growing as the system was cooling. Following

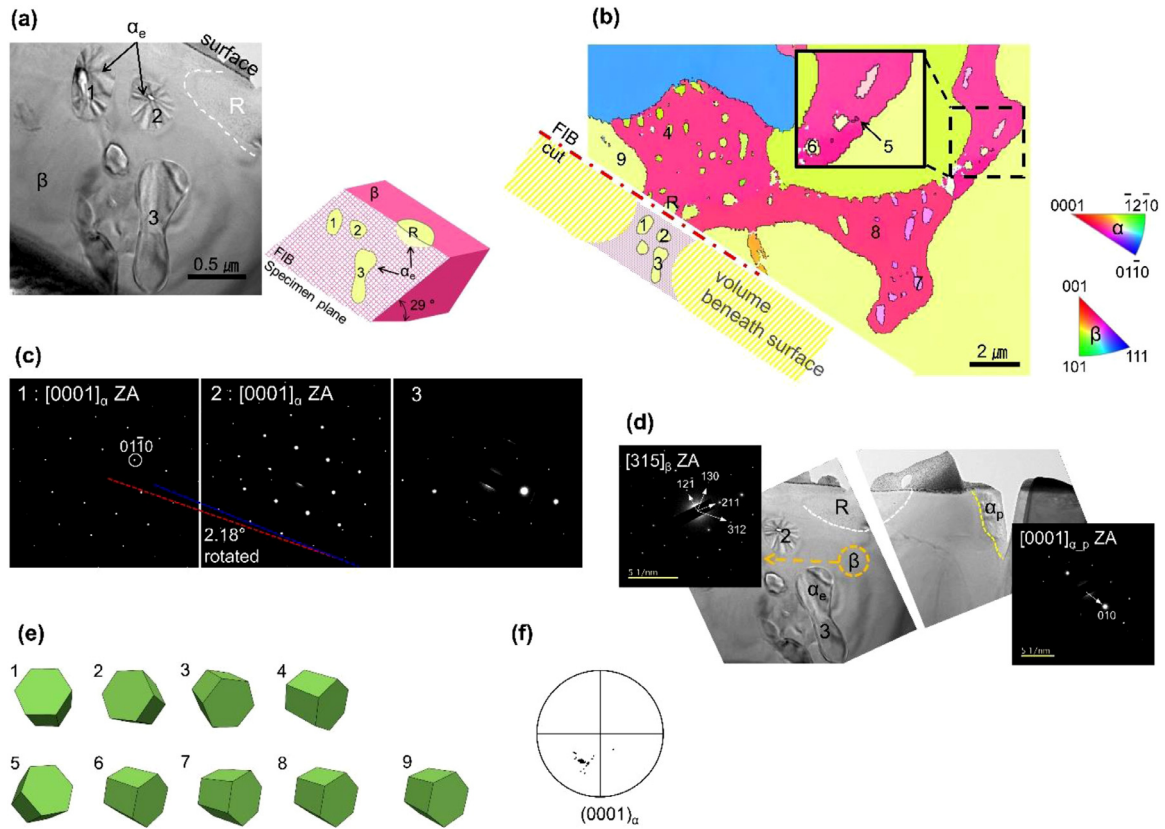


Fig. 8. The orientation analysis of the $\alpha\epsilon$ grains (points 1 to 8) with respect to the α_p grain (point 9): (a) TEM micrograph taken from beneath the surface and the schematic illustration of the FIB sampling and (b) EBSD orientation map. The dot-dashed red line indicates the FIB sectioning plane and R indicates a reference point for the FIB sampling (c) SADP of for three $\alpha\epsilon$ grains with α -tilt: -1.8° and β -tilt: -2.8° , (d) SADP of the α_p and β grains around the $\alpha\epsilon$, (e) relative orientations represented in the unit cell of the α phase, and (f) (0001) pole figure for $\alpha\epsilon$ grains from (b). (For interpretation of the references to colour in this figure legend, the reader is referred to the web version of this article.)

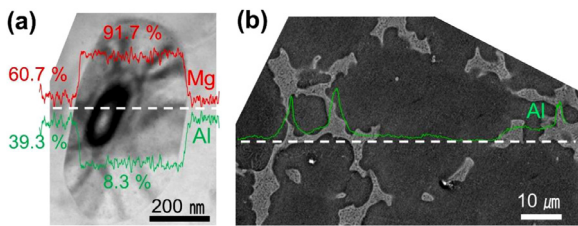


Fig. 9. Al and Mg distribution along the white dashed line measured using EDS (a) $\alpha\epsilon$ and β grains having flat concentration profiles, and (b) α_p and β grains showing smooth Al enrichment toward the dendrite growing direction. (For interpretation of the references to colour in this figure legend, the reader is referred to the web version of this article.)

the experimental observations, the nucleation density of the β phase was set to be 10 times lower than the nucleation density of the $\alpha\epsilon$ phase, and all nuclei were assigned random and uncorrelated orientation. Both the $\alpha\epsilon$ and β phases were allowed to nucleate at the same time in the entire volume of the liquid pocket if the thermodynamic driving force is sufficient to overcome their nucleation barriers set by the corresponding critical nuclei diameter. Once the undercooling is sufficient, the nucleation of the β phase occurs first, and a small number of grains begins to grow in the residual liquid as shown in Fig. 10. A strong tendency for the β phase

to grow on the perimeter of the α_p /liquid interface can be observed in Fig. 10(b), which is due to the strong segregation of Al rejected by the growing α_p . Since the solubility of Al in the α phase is lower than in the liquid, enriched Al concentration in front of the α_p dendrite results in the preferential growth of the β phase along the α_p /liquid interface. During the growth of the β phase along the α_p boundary, the cooling stops, and the temperature even increases toward the eutectic temperature due to the significant latent heat release. At the same time, the nucleation of the $\alpha\epsilon$ phase is also activated, but actual nucleation does not occur due to insufficient thermodynamic driving force. Before the onset of $\alpha\epsilon$ phase nucleation, the β phase fully covers the α_p /liquid interface as shown in Fig. 10(c) in a manner analogous to the experimental microstructure in Fig. 8(b). Thus, the simulation supports the cooperative growth of the α_p and β phases involving solutal exchange as the first stage of the eutectic solidification process. Subsequently, when the surface of α_p phase is fully covered by the β phase, further growth of α_p phase is restricted, and the remaining Al in the melt is consumed to form the β phase, reducing the Al concentration in the liquid. This brings the system into the state where the $\alpha\epsilon$ phase nucleation that completes the eutectic solidification process of the remaining liquid pockets presented in Fig. 10(d-f).

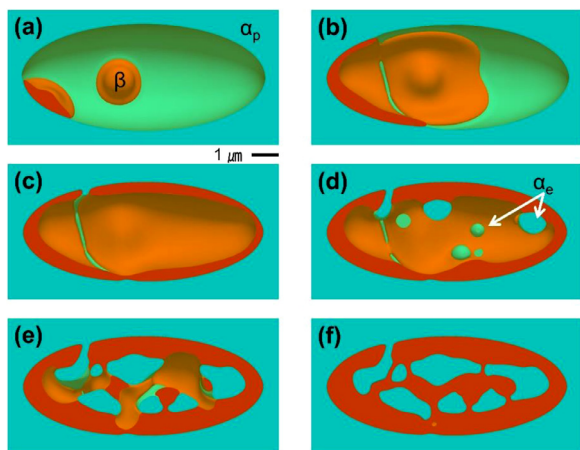


Fig. 10. Nucleation and growth of the β phase in the liquid pocket near the eutectic temperature followed by the nucleation and growth of the α_e phase in the residual liquid. (a–c) The β phase nucleates randomly in the liquid but preferentially grows along the perimeter of the α_p /liquid interface and covers it entirely. (d–f) Nucleation and growth of the α_e phase leading to complete solidification. The remaining liquid phase was colored opaque yellow. (For interpretation of the references to colour in this figure legend, the reader is referred to the web version of this article.)

4. Conclusion

The solidification morphology of the Mg–Al alloys exhibiting a (partially) divorced eutectic structure was investigated with respect to the alloy composition and the cooling rate. The results show that during the interdendritic solidification, eutectic β phase formed a closed shell around the α_p dendrite by following the Al enrichment along the α_p /liquid interface. In contrast to the prominent solutal exchange between α_p and β phases, the divorced eutectic structure followed the formation of α_e phase after rapid coverage of the α_p /liquid interface by the β phase and consequent inhibition of further growth of the α_p dendrites. The weak OR and the sharp solute concentration change between the β and α_e grains in the eutectic region suggest non-interactive nucleation and growth of a partially divorced eutectic structure in the Mg–10%Al alloy. The experimental findings were supported by the phase-field simulations which are in good agreement. The phase-field simulation successfully depicts the formation of the β phase halo on the α_p interdendritic perimeter and partially divorced eutectic microstructure consistent with the experimental observations.

Acknowledgement

This research is supported by the Fundamental Research Program of Korea Institute of Materials Science (PNK7760 and PNK7770) and the National Research Foundation of Korea (2020R1A2C2008416 and 2021M3H4A6A01049712).

References

- [1] S. Barbagallo, H.I. Laukli, O. Lohne, E. Cerri, J. Alloys Compd. 378 (2004) 226–232, doi:10.1016/j.jallcom.2003.11.174.
- [2] A.K. Dahle, Y.C. Lee, M.D. Nave, P.L. Schaffer, D.H. StJohn, J. Light Metals 1 (2001) 61–72, doi:10.1016/S1471-5317(00)00007-9.
- [3] M.S. Dargusch, M. Nave, S.D. McDonald, D.H. StJohn, J. Alloys Compd. 492 (2010) L64–L68, doi:10.1016/j.jallcom.2009.11.199.
- [4] M.D. Nave, A.K. Dahle, D.H. StJohn, Eutectic growth morphologies in magnesium–aluminium alloys, in: H.I. Kaplan, J. Hryn, B. Clow (Eds.) 2000 TMS Annual Meeting, The Minerals, Metals, & Materials Society, Nashville, TN, 2000, pp. 233–242.
- [5] T. Zhu, Z.W. Chen, W. Gao, J. Alloys Compd. 501 (2010) 291–296, doi:10.1016/j.jallcom.2010.04.090.
- [6] D. Amberger, P. Eisenlohr, M. Goeken, Acta Mater 60 (2012) 2277–2289, doi:10.1016/j.actamat.2012.01.017.
- [7] M. Joansson, D. Thierry, N. LeBozec, Corros. Sci. 48 (2006) 1193–1208, doi:10.1016/j.corsci.2005.05.008.
- [8] J. Zhang, J. Xu, W. Cheng, C. Chen, J. Kang, J. Mater. Sci. Technol. 28 (2012) 1157–1162 (Shenyang, China), doi:10.1016/S1005-0302(12)60186-8.
- [9] M. Mexbahul-Islam, A.O. Mostafa, M. Medraj, J Mater (2014) 2014Article ID 704283, doi:10.1155/2014/704283.
- [10] D.A. Porter, K.E. Eastering, Taylor & Francis, Boca Raton, 2004 2nd ed.
- [11] E. Borukhovich, M. Boeff, A. Monas, M. Tegeler, S.-J. Kim, C.-S. Oh, I. Steinbach, MATEC Web Conf 80 (2016) 02014, doi:10.1051/mateconf/20168002014.
- [12] A. Monas, O. Shchyglo, D. Hche, M. Tegeler, I. Steinbach, IOP Conf. Ser.: Mater. Sci. Eng. 84 (2015) 012069, doi:10.1088/1757-899X/84/1/012069.
- [13] A. Monas, O. Shchyglo, S.-J. Kim, C.D. Yim, D. Hche, I. Steinbach, JOM 67 (2015) 1805–1811, doi:10.1007/s11837-015-1418-4.
- [14] I. Steinbach, Modell. Simul. Mater. Sci. Eng. 17 (2009) 073001, doi:10.1088/0965-0393/17/7/073001.
- [15] B. Boettger, J. Eiken, I. Steinbach, Acta Mater 54 (2006) 2697–2704, doi:10.1016/j.actamat.2006.02.008.
- [16] A.L. Greer, A.M. Bunn, A. Tronche, P.V. Evans, D.J. Bristow, Acta Mater 48 (2000) 2823–2835, doi:10.1016/S1359-6454(00)00094-X.
- [17] Thermo-Calc, Thermo-Calc Software TCMG2 Mg-alloys database (accessed 2 July 2019), in 2019.
- [18] J.O. Anderssoon, T. Helander, L. Höglund, P.F. Shi, B. Sundman, Calphad 26 (2002) 273–312, doi:10.1016/S0364-5916(02)00037-8.
- [19] S. Akamatsu, M. Plapp, Curr. Opin. Solid State Mater. Sci. 20 (2016) 46–54, doi:10.1016/j.cossms.2015.10.002.
- [20] S. Ji, Z. Fan, Metall. Mater. Trans. A 40 (2009) 185–195, doi:10.1007/s11661-008-9713-0.
- [21] Y. Wang, H. Jones, P.V. Evans, J. Mater. Sci. 33 (1998) 5205–5220, doi:10.1023/A:1004483904519.
- [22] S. Celotto, TEM study of continuous precipitation in Mg–9wt%Al–1wt%Zn alloy, Acta Mater., 48 (2000) 1775–1787, doi:10.1016/S1359-6454(00)00004-5.
- [23] U. Dahmen, Acta Metall 30 (1982) 63–73, doi:10.1016/0001-6160(82)90045-1.
- [24] H. Liu, J. Liu, L. Ouyang, C. Luo, J. Appl. Crystallogr. 45 (2012) 224–233, doi:10.1107/S002188981200091X.
- [25] M.-X. Zhang, P.M. Kelly, Scr. Mater. 48 (2003) 647–652, doi:10.1016/S1359-6462(02)00555-9.
- [26] S. Guldberg, N. Ryum, Mater. Sci. Eng., A 289 (2000) 143–150, doi:10.1016/S0921-5093(00)00945-X.